Light absorption by surface nanoholes and nanobumps

A Rudenko, C. Mauclair, F. Garrelie, R. Stoian, Jean-Philippe Colombier

Accepted Manuscript

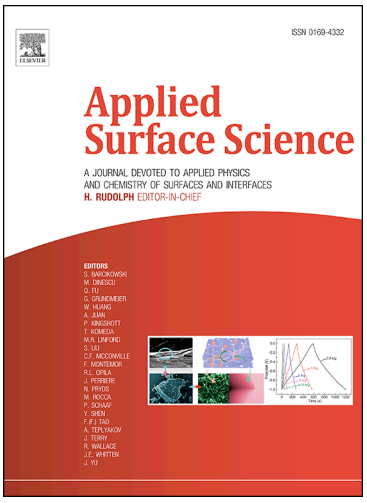

Full Length Article

Light absorption by surface nanoholes and nanobumps

A. Rudenko, C. Mauclair, F. Garrelie, R. Stoian, J.P. Colombier

PII: S0169-4332(18)33190-8
DOI: https://doi.org/10.1016/j.apsusc.2018.11.111
Reference: APSUSC 40957

To appear in: *Applied Surface Science*

Received Date: 31 August 2018
Accepted Date: 14 November 2018

Please cite this article as: A. Rudenko, C. Mauclair, F. Garrelie, R. Stoian, J.P. Colombier, Light absorption by surface nanoholes and nanobumps, *Applied Surface Science* (2018), doi: https://doi.org/10.1016/j.apsusc.2018.11.111

Light absorption by surface nanoholes and nanobumps

A. Rudenko[a], C. Mauclair[a], F. Garrelie[a], R. Stoian[a], J. P. Colombier[a,*]

[a] *Univ Lyon, UJM-Saint-Etienne, CNRS, IOGS, Laboratoire Hubert Curien UMR5516, F-42023 St-Etienne, France*

Abstract

This paper deals with a numerical investigation of the energy deposition induced by ultrafast laser interaction with nanostructures. We calculate and analyze the intensity near-field reactive and radiative patterns resulted from the interference of the incident light with light scattered by individual subwavelength holes and bumps on the surface of metallic and dielectric materials. The role of light polarization, optical material properties, collective effects and nature of the imperfections in localized energy absorption is elucidated. The results open new perspectives in precise light manipulation by surface inhomogeneities and well-controlled surface nanostructuring by ultrashort laser.

1. Introduction

Light interaction with basic surface nanostructures, such as holes and ridges, lies at the heart of subwavelength optics, signal processing on the nanoscale, nanophotonics and nanoplasmonics. The presence of these tiny imperfections has been proved to modify the optical properties of the pristine material, contributing to strongly enhanced transmission, anomalous optical absorption, wavelength filtering, and surface plasmon wave excitation on metal surfaces [1–9]. Efficient light manipulation on the nanoscale is hence possible nowadays by using optical devices, where diffraction gratings or nanoslits, periodic arrangements of holes or nanoparticles serve as general counterparts. Control over the optical response of such devices requires precise knowledge of the interference patterns and field distributions in the vicinity of individual nanoobjects. Even if the near-field optical microscopy is already able to reconstruct the complete interference maps with nanoscale resolution [10, 11], the understanding of the involved electromagnetic phenomena is possible only via rigorous theoretical or numerical analysis.

The energy absorption maps on the surfaces are particularly required to understand laser interaction with matter, because the patterns of maximum absorbed energy define precisely the thermo-affected zones, where the material modification such as ablation is likely to take place after the energy deposition [12–19]. This way, the laser-affected surface can be efficiently treated pulse by pulse. The modifications strongly influence the surface roughness and the energy deposition below the surface [18, 20], therefore, it appears crucial to predict in which way the absorbed energy profiles change. Self-organization of polarization-dependent periodic surface nanostructures is among the impressive phenomena induced by multipulse ultrashort laser irradiation [17, 18, 21, 22].

Light scattering by surface inhomogeneities has been intensively studied theoretically. For instance, the expanded Mie solutions [23, 24] were obtained for the scattered fields of a single subwavelength spherical nanoparticle near and on the perfectly conducting surface [25, 26]. However, the analytical solution is complicated in case of metal or lossy interface, as well as the arbitrary sizes of the inhomogeneity (hole or bump) due to the non-trivial boundary conditions at the sphere (or half-sphere) and plane surface, which should be satisfied simultaneously. The charge accumulation at the edges of the imperfection results in the phase retardation of the scattered wave, and, therefore, different spatial energy localization [27–29]. Only the semi-analytical dipole approximations for the scattered fields are known in this case [30, 31], whereas the

*Corresponding author
Email address: jean.philippe.colombier@univ-st-etienne.fr (J. P. Colombier)

general problem requires calculation of Sommerfeld's integrals over all diffraction modes [32]. The alternative way consists in treating the electromagnetic problem numerically based on the complete solution of three-dimensional Maxwell's equations.

In this paper, we investigate numerically the energy absorption below dielectric and metallic surfaces with a single or several holes or ridges and analyze the influence of light polarization, optical properties of material, and arbitrary shape of nanoobjects on the resulting scattered radiative and non-radiative fields. For this, we solve a full system of Maxwell's equations by Finite-Difference Time-Domain approach [33, 34], which was successfully used for scattering, transmission and absorption data analysis in case of subwavelength individual, periodic and randomly distributed holes and bumps on the surface [17, 18, 21, 22, 28, 35, 36]. We focus on two different materials, widely used in industry: unexcited fused silica glass (dielectric) and stainless steel (metal).

2. Modeling details

The system of three-dimensional Maxwell's equations is solved

$$\begin{cases} \dfrac{\partial \vec{E}}{\partial t} = \dfrac{\nabla \times \vec{H}}{\epsilon_0 \epsilon_\infty} - \dfrac{1}{\epsilon_0 \epsilon_\infty} \vec{J} \\ \dfrac{\partial \vec{H}}{\partial t} = -\dfrac{\nabla \times \vec{E}}{\mu_0}, \end{cases} \tag{1}$$

where $\vec{E}$ is the electric field, $\vec{H}$ is the magnetizing field, and $\vec{J}$ is the electric current density, μ_0 is the permeability of free space, ϵ_0 is the free space permittivity, and ϵ_∞ is the value of material permittivity at infinite frequency. Drude model is incorporated to model the properties of the materials. The equation for $\vec{J}$ current is solved to include the dispersion of the optical properties in (1) via the auxiliary differential equation method [34]

$$\frac{\partial \vec{J}}{\partial t} + \vec{J}/\nu = \epsilon_0 \omega_{pl}^2 \vec{E}, \tag{2}$$

where ω_{pl} is the plasma frequency, and ν is the collision frequency. At the edges of the grid, absorbing boundary conditions related to convolutional perfect matched layers (CPML) are set to avoid non-physical reflections [37].

Laser wavelength is fixed to be $\lambda = 800$ nm. The refractive index and the extinction coefficients for stainless steel are taken $n = 2.57$ and $k = 3.12$, whereas the refractive index of fused silica glass is $n = 1.45$. For stainless steel, the effective values for the collision frequency $\nu = 9.15 \cdot 10^{15}$ Hz and for the plasma frequency $\omega_{pl} = 19.2 \cdot 10^{15}$ Hz are deduced from Drude formula approximation for real and imaginary parts of permittivity and the known refractive indices as $\nu = 2nk\omega(1 - n^2 + k^2)$ and $\omega_{pl}^2 = (\omega^2 + \nu^2)(1 - n^2 + k^2)$, where $\omega = 2\pi c/\lambda$ is the laser frequency. The dispersion-less model is used for unexcited glass with $\epsilon_\infty = n^2$. The influence of transient optical properties on the energy distribution under strong excitation of dielectrics is beyond the scope of this article, but was previously addressed in Refs. [17, 38]. Holes and bumps are half-spheres with radius $R = 20$ nm. Both holes and bumps are centered at $(0, 0, 0)$ positions.

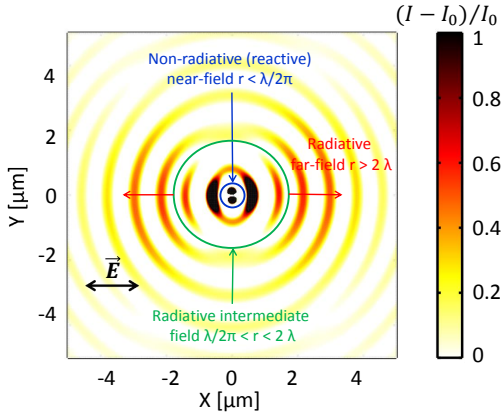

Figure 1: Classification of interference patterns resulted from scattering by a single nanohole on metal surface.

An ultra-short Gaussian pulse is introduced as the linear-polarized electric field excitation source

$$E_x(t, r, z) = \frac{w_0}{w(z)} \exp\left[-\frac{(t - t_0)^2}{\tau^2}\right] \cdot \\ \cdot \exp\left[-\frac{r^2}{w(z)^2} - ikz - ik\frac{r^2}{2R(z)} + i\varsigma(z)\right], \tag{3}$$

where $\tau = 80$ fs is the pulse width at half maximum (FWHM), $t_0 = 160$ fs is the time delay, $w_0 = 10\mu m$ is the beam waist radius, $w(z) = w_0\sqrt{1 + (\frac{z}{z_R})^2}$ is the Gaussian's beam spot size, $z_R = \pi {w_0}^2 n_0/\lambda$ is the Rayleigh length, $r = x^2 + y^2$ is the radial distance from the beam's waist, $R(z) = z[1 + (\frac{z_R}{z})^2]$ is

the radius of curvature of the beam's wavefront, and $\varsigma(z) = \arctan(\frac{z}{z_R})$ is the Gouy phase shift. The effects of the finite spectral bandwidth in case of extremely short laser pulses $\tau < 40$ fs is also investigated in the article, considering temporally-dependent dispersion $\Delta\lambda$.

Light propagates along $0z$ axis, whereas the light polarization is along $0x$ axis. This way, $x0z$ is the propagation plane and $x0y$ is the transverse plane perpendicular to light wave-vector $\vec{k}$. In most cases, the time-integrated intensity distribution inside material (stainless steel or glass) $I = \frac{n}{2}\sqrt{\frac{\epsilon_0}{\mu_0}}\left|\vec{E}\right|^2$ is represented in the figures. This value is proportional to the absorbed energy further transferred to the material via Joule heating. In Figs. 4-5 and Figs. 8-9, the intensity in normalized to the maximum incident value of the electric field E_0. This way, the value $(I - I_0)/I_0$ indicates the intensity enhancement, from which the incident field is extracted for clarity.

We define different regimes of scattering as a function of distance from the object under consideration as indicated in Fig. 1 in case of a single nanohole on metal surface. The closest near-field region includes non-radiative patterns, for which the electric field is confined to the edges of the nanoobject. The boundary between radiative and non-radiative fields classically corresponds to the distance $r = \lambda/2\pi$, where the contributions with amplitudes decaying proportional to $1/r$ and $1/r^3$ of an isolated electric dipole are equal [24]. The intermediate region $\lambda/2\pi < r < 2\lambda$ is the transition zone between near-field and far-field radiative scattering.

The electric fields of both non-radiative and radiative patterns are directly accessed via FDTD, without applying the near-to-far-field transform. In this work, we are mainly interested in absorption on surfaces irradiated by a focused laser pulse but not in reflection characteristics. Therefore, the analysis is limited to the region of few laser wavelengths, where the absorption is the highest, including both non-radiative and radiative interference patterns. The scattered fields at distances farther than few wavelengths have repetitive behavior and can be intuitively reproduced by taking account the decay of the surface wave and the wavefront transformation from quasi-spherical to planar or by applying near-to-far-field transformations [34, 39, 40].

3. Non-radiative near-field patterns

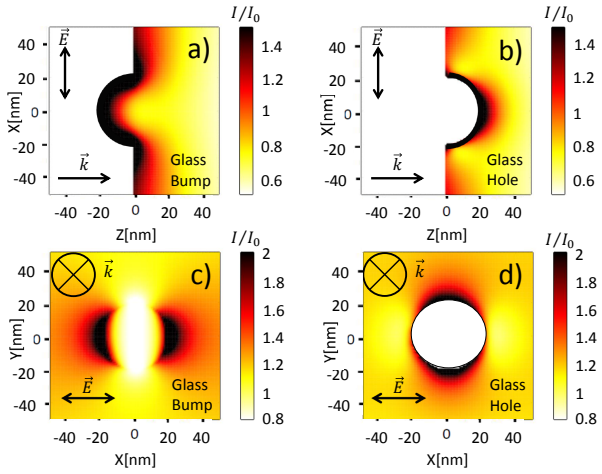

Figure 2: Energy deposition below glass surface in the propagation plane (a) with a bump $R = 20$ nm, (b) with a hole $R = 20$ nm and in the transverse plane on the surface (c) with a bump $R = 20$ nm, (d) with a hole $R = 20$ nm.

Fig. 2 shows the intensity distribution on a glass surface in the propagation (a, b) and in the transverse planes (c, d). In case of a bump on dielectric surface, the energy is equally deposited on the top of the bump and on both edges of the equatorial plane intersecting the surface. Therefore, the peaks of the nanometric bumps are likely to be erased by laser ablation. The local field enhancement results in the maxima parallel and minima perpendicularly to light polarization in the transverse plane. In case of a nanometric hole on dielectric surface, the energy is mostly deposited inside the hole. In this case, the maxima of local field are perpendicular to laser polarization. This way, the material ablation with holes leads to more pronounced deeper holes and the reinforcement of polarization dependency of the absorbed energy below dielectric surface. The polarization dependency of the intensity maxima can be understood by a simple analogy with Mie theory. In fact, hole on glass surface owns the properties of matter with smaller refractive index inside the material with greater one. In contrast, the properties of bump below the surface result from the continuous prolongation of the electric field above the surface, where a particle of glass (bump) is surrounded by air, therefore, matter with larger refractive index embedded in medium with smaller refractive index. Regarding Fig. 2(c)

and Fig. 2(d), the minor nanometric change in surface morphology results in contrasting switching of polarization-dependent near-field optical response.

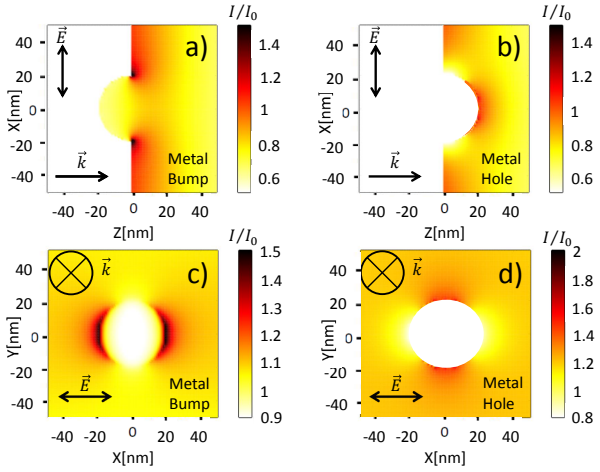

Figure 3: Energy deposition below metal surface in the propagation plane (a) with a bump $R = 20$ nm, (b) with a hole $R = 20$ nm and in the transverse plane (c) with a bump $R = 20$ nm, (d) with a hole $R = 20$ nm.

Fig. 3 demonstrates the intensity distribution below a metallic surface. One of the principle difference with glass is that the energy is no more deposited on the top of the metallic bump but only on the surface dominantly in the direction parallel to laser polarization. This result indicates that the laser ablation not necessarily erases the bump, but rather yields a more pronounced imperfection. The formation mechanisms of laser-induced bump-like bubble crescents and cone-shaped nanovolcanoes on thin titanium films have been recently investigated and the dominant vertical modes of the structures at normal incidence irradiation have been successfully applied to color marking [8]. The energy is still deposited mostly inside the nanometric hole, and similar dependencies of local field maxima perpendicular to laser polarization for stainless steel are revealed in Fig. 3(b, d). Therefore, the material ablation favors the formation of deep ellipsoidal holes elongated perpendicular to laser polarization. The light interaction with non-symmetrical imperfections is investigated further in the manuscript.

The above results remain qualitatively accurate for sizes of holes and bumps smaller than the wavelength of light $R < \frac{\lambda}{2\pi}$.

4. Radiative and non-radiative responses

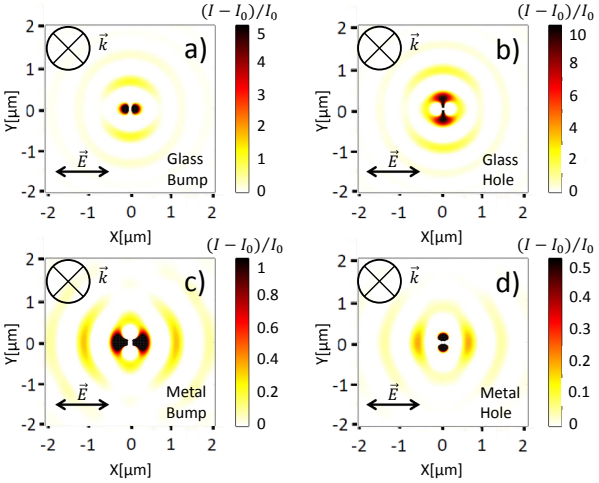

Figure 4: Absorbed energy in the transverse plane on glass surface with (a) a bump, (b) a hole and on metal surface with (c) a bump, (d) a hole of $R = 20$ nm. Light interaction exhibit contrasting polarization-sensitive interference patterns (in the micrometer scale) depending on the optical material properties and the nature of imperfections.

Fig. 4 shows the main features of both radiative and non-radiative fields scattered by subwavelength imperfections on the surface. The interference patterns are more pronounced in perpendicular direction to light polarization on glass surface and in parallel direction on metal surface. In contrast to local near-field, the orientation of the radiative patterns does not depend on the nature of the imperfections (compare Fig. 4(a) with Fig. 4(b) and Fig. 4(c) with Fig. 4(d)). The striking difference is revealed, however, in the distances between the intensity maxima positions and the emission centers. This fact is related to different phase retardation of surface waves scattered by holes and bumps. This way, the first far-field maxima (to differ between the local near-field) are on the greater distance from the hole than from the bump for glass surface and from the bump than from the hole for metal surface. Note that the difference is related directly to charge accumulation on the interface of imperfection and, therefore, to local near-field distributions. For glass, the interference patterns represent spherical standing waves with λ/n spacings in Fig. 4(a, b), whereas for metal the symmetry is broken due to additional contribution of surface plasmon wave in the direction parallel to the electric field with spacings $\approx \lambda$ in Fig. 4(c, d). The

absorbed energy maps, however, do not allow us to separate the contribution of surface plasmon wave from so-called quasi-cylindrical wave [30]. This fact will be discussed further in the article. In case of holes on thin metallic films, the near-field optical microscopy was applied to observe the radiative interference patterns similar to ones calculated in Fig. 4(d) [10, 11].

Interestingly, Fig. 4 evidences the symmetry principle of scattering by nanoholes and nanobumps of equivalent size. If we superpose the interference patterns either in Figs. 4(a, b) or in Figs. 4(c, d), we can note that they are more pronounced for hole for locations where they are less pronounced for bump.

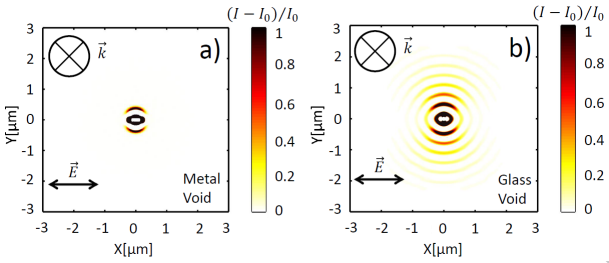

Figure 5: Absorbed energy below stainless steel surface in the transverse plane with an intrinsic void of $R = 20$ nm at 50 nm below (a) metal surface and (b) glass surface. The optical response of nanovoids inside the material varies from the response of surface imperfections in Fig. 4.

The presence of intrinsic imperfections also influences the field distribution below the surface [18]. The response of such intrinsic voids is completely different from surface holes and bumps and can be understood by Mie theory for a spherical nanoparticle in media. The resulting interference patterns calculated by FDTD are shown in Fig. 5 for intrinsic voids inside but near metal and glass surfaces. The non-radiative fields are qualitatively similar for the imperfections of different nature. Regarding the radiative field, the maxima of the absorbed energy correspond to the positions in the direction perpendicular to polarization in both cases of metal and glass surface. The spherical wave has, however, different decays as the distance from the emission center changes. The surface wave decays faster in case of metal due to non-negligible extinction coefficient and significant losses. This way, only the first intensity maxima is visible. In case of glass, the decay of periodic patterns with characteristic λ/n spacings is only due to radiative losses and is similar to the optical response of a hole on a glass surface.

5. Nature of the surface waves

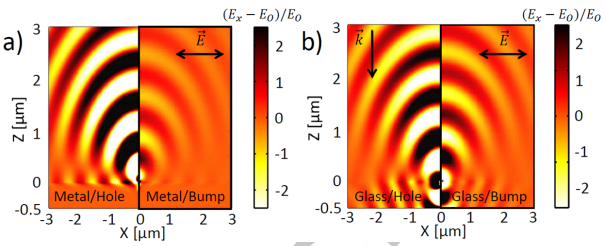

Figure 6: Electric field E_x distribution in the air and below the surface in the propagation plane in case of hole/bump (a) on metal surface and (b) on glass surface. The figures are brought together in order to show the phase difference and the symmetry principle of the response of bumps and holes.

Some additional information can be accessed via FDTD by analyzing the electric field distributions in the propagation plane. Recently, the nature of surface waves responsible for the electric field maxima has been intensively debated in the literature [30, 31]. The semi-analytical approaches considering the scattered fields of a dipole on metal-air interface indicate that the total scattered field is the sum of surface plasmon and quasi-cylindrical wave contributions [30, 31]. The behavior of surface plasmon wave near metal-air interface is well-known, particularly the strong exponential decay with the distance from the interface in the air and in the metal. In contrast, the quasi-cylindrical wave decays more slowly and can still propagate in the air. This way, the total electric field distribution in Fig. 6(a) shows that both of waves exist on metal-air interface and are phase-shifted. The nature of this phase-shift has been previously discussed in terms of surface wave retardation due to charge accumulation at the edges of hole or bump [27]. In case of glass surface, there is no mismatch in Fig. 6(b), because the condition of surface plasmon wave excitation is not satisfied, therefore, only the quasi-cylindrical surface wave contributes to the total scattered electric field.

Interestingly, different surface topography results in different shifts and electric field maxima positions regarding the emission center. Fig. 6 clearly demonstrates the symmetry principle both for metal and glass surface imperfections. Disregarding the fact that the amplitude of scattered field from the hole is greater than for the bump, the electric fields of opposite imperfections are out of phase by π and, therefore, compensate each other.

6. Finite spectral bandwidth

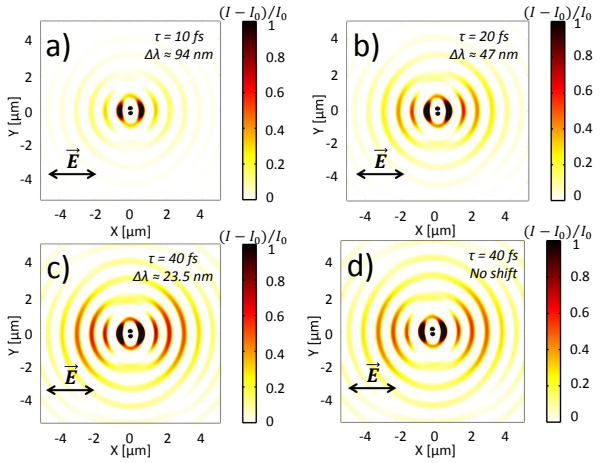

Figure 7: Influence of finite spectral bandwidth on the interference patterns in the vicinity of a single nanohole on metal surface. The considered pulse durations and wavelength dispersion are indicated in each sub-figure (a-d).

The shorter the femtosecond pulse is, the larger the spectral bandwidth, defined as $\Delta\lambda = \lambda\frac{\Delta\omega}{\omega} = \frac{2\ln 2}{\pi c\tau}\lambda^2$ for a Gaussian pulse. This way, one obtains $\Delta\lambda \approx 94.08$ nm for $\tau = 10$ fs with bandwidth centered to $\lambda = 800$ nm. The other two factors that potentially influence the interference patterns are the changes in refractive indices due to the presence of multiple wavelengths and the pulse duration itself - the number of optical cycles (one optical cycle is ≈ 2.67 fs). We investigate the influence of these factors on the basic interference patterns from a nanohole on metal surface. Firstly, we check that the refractive index changes (the refractive index dependence on wavelength is taken from Ref. [41] for Fe) do not play a significant role even quantitatively. Then, we verify that the similar interference patterns with similar decay and amplitude can be obtained for one or two-cycle pulses without taking into account the dispersion and keeping unchanged the fluence. Hence, the limited distance of scattered wave propagation from the object due to short pulses does not affect the radiative interference patterns up to few microns from the object. Finally, we investigate the impact of dispersion $\lambda \pm \Delta\lambda$, by simulating Gaussian pulse with temporally dependent wavelength. The results for 10 fs, 20 fs and 40 fs are shown in Fig. 7 and compared with the interference patterns in case of fixed wavelength equal to $\lambda = 800$ nm. The fluence is kept unchanged for different pulse durations. The radiative interference patterns are similar in case of 40 fs pulse, but change quantitatively and become less pronounced for shorter pulses of 10 fs and 20 fs in Fig. 7(a, b). Therefore, the temporal pulse broadening results in a smaller amplitude produced by the central wavelength and lower absorbed energy on the surface. The visible interference patterns in Fig. 7(a, b) are still the result of the interaction mostly with central wavelength of laser pulse, but the patterns are more dispersed and less pronounced due to the presence of other shifted wavelengths. Furthermore, both quasi-cylindrical and surface plasmon waves are affected, because the intensity is reduced in both perpendicular and parallel direction to laser polarization. The influence of finite spectral bandwidth on resonant surface plasmon excitation by prism coupling technique was previously measured and investigated [42].

7. Elongated and random topographies

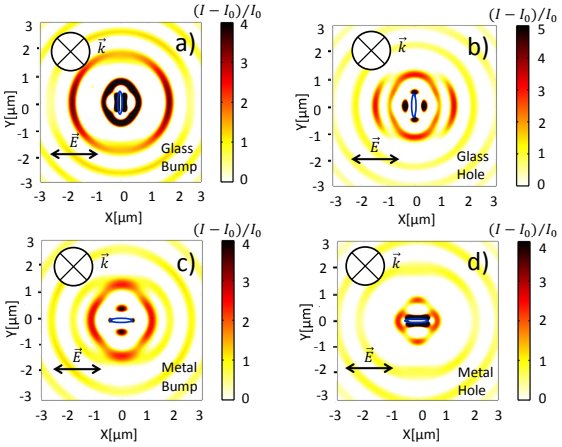

Figure 8: Absorbed energy in the transverse plane on glass surface (a) with a nanoridge of $R_x = R_z = 20$ nm and $R_y = 500$ nm or (b) with a nanoslit above the surface $R_x = R_z = 20$ nm and $R_y = 500$ nm. Absorbed energy in the transverse plane below metal surface (c) with a nanoridge of $R_y = R_z = 20$ nm and $R_x = 500$ nm or (d) with a nanoslit above the surface $R_y = R_z = 20$ nm and $R_x = 500$ nm. For clearness, the imperfection positions centered at $(0, 0, 0)$ are indicated by blue ellipsoids. The interference patterns qualitatively differ from the corresponding ones in Fig. 4.

Fig. 4 indicates that the polarization-dependent orientation of the maxima of radiative patterns are mostly subject of the material properties, whereas the nature and the arbitrary size or shape of the imperfection do not play a key role. However, this re-

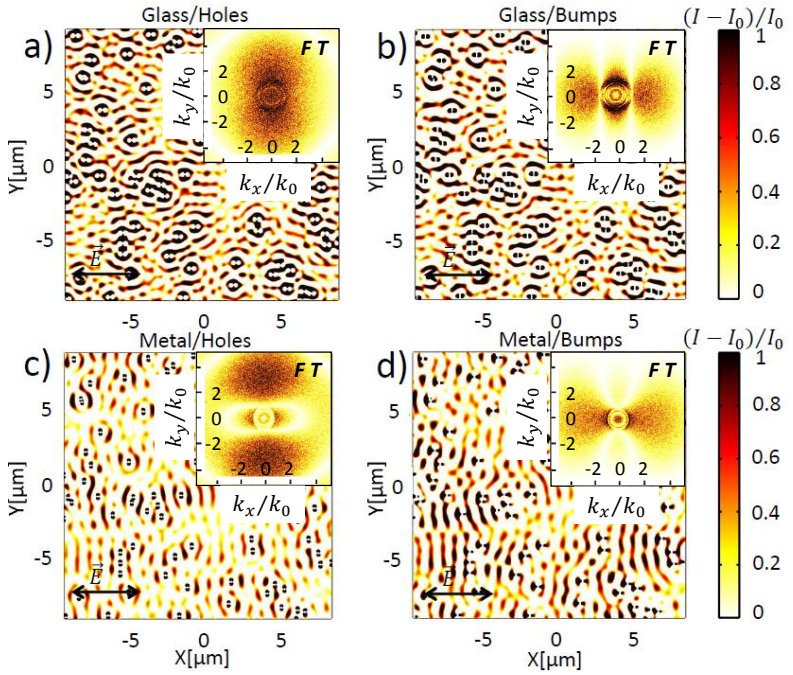

Figure 9: Absorbed energy distributions and their Fourier Transforms (FT) in the transverse plane on glass surface with (a) holes, (b) bumps and on metal surface with (c) holes, (d) bumps of $R = 20$ nm. $k_0 = 2\pi/\lambda$ is the wave-vector of propagation in air.

mains true only if the size of hole or bump is smaller than wavelength and its shape is symmetrical. For instance, Fig. 8 shows that the maxima of the electric field in the direction parallel to the electric field polarization on metal surface or in the direction perpendicular to the electric field on glass surface can be significantly enhanced if the imperfection has an ellipsoidal shape and a length approaching to laser wavelength. For instance, the closest intensity maxima to imperfections switch from parallel (typical to subwavelength symmetrical holes or bumps as in Fig. 4(a, b)) to perpendicular positions on glass surface in Fig. 8(a, b). In contrast, the closest intensity maxima switch from perpendicular (as in Fig. 4(c, d)) to parallel positions on metal surface as shown in Fig. 8(c, d). These features have consequences in multipulse irradiation, where evolving surface topography or deformation centers influence the feedback process [17]. The introduction of artificial supra-wavelength scattering objects on the surface, such as elongated nanoridges and nanoslits, affects not only the dominant pattern configuration, but also results in more regular planar wavefront of the scattered waves [12, 13, 19]. Our calculations indicate, however, that the origin of these waves is mixed depending on the structure geometry and, therefore, on Mie scattering or previously mentioned quasi-cylindrical waves on the surface, optical properties of the media (metal or glass), and, where the conditions are satisfied, additional contribution of surface plasmon wave for metal surfaces, as proposed in Refs. [12, 19]. Similar geometrical effects from more complexed structures such as microtriangles and microsquares with imprinted patterns oriented both perpendicular and parallel to laser polarization were observed experimentally [14].

Fig. 9 shows the interference patterns as a result of light interaction with randomly distributed holes and bumps below glass and metal surfaces. For simplicity, we choose the identical positions of the imperfections with the same concentration $C = 0.5\%$ or the same average inter-object distance $d \approx 1.5\mu m$ on $x0y$ transverse plane in all the cases in Fig. 9. The resulting absorption maps are the consequences of the coherent response of individual bumps and holes from Fig. 4, therefore, the features regarding polarization dependency of radiative and non-radiative fields remain qualitatively the same. The coherence here plays an important

role as the patterns result from the interference of the same incident field with the scattered surface waves [22]. The coupling effects, however, are almost negligible for the average distances between imperfections exceeding the laser wavelength. This fact is clearly seen from Fourier Transforms (FT) of the corresponding images. The response from radiative fields there corresponds to smaller wave-vectors, whereas the non-radiative fields are characterized by more dispersed frequency profiles with larger values of wave-vectors. The radiative field patterns on metal surface are straight perpendicular to laser polarization, whereas the patterns on glass surface conserve more pronounced properties of spherical waves, having the dominant orientation parallel to laser polarization. The average spacings on metal surface correspond to $\approx \lambda$ (or $k_x/k_0 \approx 1$ on FT), whereas the average spacings on glass surface are close to λ/n (or $k_y/k_0 \approx 1.5$ on FT). Again, the symmetry principle regarding the energy absorption by holes and bumps can be applied for complex systems as in Fig. 9.

The quasi-periodic interference patterns induced by nanoscale surface imperfections have been previously proposed to explain the formation mechanism of laser-induced periodic surface structures with periods of λ/n parallel to electric field polarization on dielectric surfaces, with periods of λ perpendicular to electric field polarization on metal surfaces, as well as periods significantly smaller than laser wavelength [18, 21, 22]. Our article completes the previous investigations by summarizing the variety of polarization-dependent interference patterns with different orientations depending on the nature of imperfections, their shape and position regarding the surface.

8. Conclusion

We have numerically investigated the energy deposition below the surface by light interaction with single holes and bumps. This study provides qualitative and quantitative estimations of the scattered radiative and non-radiative patterns below metallic and dielectric surfaces. Among interesting peculiarities of light interaction with imperfections, we can underline the main following observations

(1) inverse local non-radiative field response of nanoholes and nanoridges, controllable by light polarization;

(2) inverse radiative response of imperfections depending on optical material properties (metal, dielectric);

(3) inversion of absorbed energy maxima position for surface nanoholes and intrinsic voids close to metal surface;

(4) different phase retardation and position of absorbed energy maxima for metal nanobumps and nanoholes on metal surfaces;

(5) less pronounced interference patterns for femtosecond pulses shorter than 40 fs due to finite spectral bandwidth;

(6) switching of absorbed energy maxima position in case of elongated imperfections of near-wavelength size;

(7) joint interference patterns as a result of collective response of imperfections.

This study provides original ideas towards nanoscale design of surfaces, optimal laser-induced nanostructuring and nanolithography, precise light manipulation by surface imperfections, and fabrication of polarization-sensitive devices.

Acknowledgments

This work was supported by IMOTEP project within program 'Investissements d'Avenir' operated by ADEME.

References

[1] T. W. Ebbesen, H. J. Lezec, H. F. Ghaemi, T. Thio, P. A. Wolff, Extraordinary optical transmission through sub-wavelength hole arrays, Nature 391 (6668) (1998) 667.

[2] C. Genet, T. W. Ebbesen, Light in tiny holes, Nature 445 (7123) (2007) 39–46.

[3] J. Le Perchec, P. Quemerais, A. Barbara, T. Lopez-Rios, Why metallic surfaces with grooves a few nanometers deep and wide may strongly absorb visible light, Physical Review Letters 100 (6) (2008) 066408.

[4] D. K. Gramotnev, S. I. Bozhevolnyi, Plasmonics beyond the diffraction limit, Nature Photonics 4 (2) (2010) 83–91.

[5] T. Coenen, A. Polman, Optical properties of single plasmonic holes probed with local electron beam excitation, ACS Nano 8 (7) (2014) 7350–7358.

[6] A. Kuchmizhak, O. Vitrik, Y. Kulchin, D. Storozhenko, A. Mayor, A. Mirochnik, S. Makarov, V. Milichko, S. Kudryashov, V. Zhakhovsky, et al., Laser printing of resonant plasmonic nanovoids, Nanoscale 8 (24) (2016) 12352–12361.

[7] X. Wang, A. Kuchmizhak, D. Storozhenko, S. Makarov, S. Juodkazis, Single-step laser plasmonic coloration of metal films, ACS Applied Materials & Interfaces 10 (1) (2017) 1422–1427.

[8] D. Hu, Y. Lu, Y. Cao, Y. Zhang, Y. Xu, W. Li, F. Gao, B. Cai, B.-O. Guan, C.-W. Qiu, X. Li, Laser-splashed three-dimensional plasmonic nanovolcanoes for steganography in angular anisotropy, ACS Nano 12 (9) (2018) 9233–9239.

[9] J.-M. Guay, A. Cal Lesina, J. Baxter, G. Killaire, L. Ramunno, P. Berini, A. Weck, Topography tuning for plasmonic color enhancement via picosecond laser bursts, Advanced Optical Materials 6 (17) (2018) 1800189.

[10] L. Yin, V. K. Vlasko-Vlasov, A. Rydh, J. Pearson, U. Welp, S.-H. Chang, S. K. Gray, G. C. Schatz, D. B. Brown, C. W. Kimball, Surface plasmons at single nanoholes in Au films, Applied Physics Letters 85 (3) (2004) 467–469.

[11] D. V. Permyakov, I. S. Mukhin, I. I. Shishkin, A. K. Samusev, P. A. Belov, Y. S. Kivshar, Mapping electromagnetic fields near a subwavelength hole, JETP Letters 99 (11) (2014) 622–626.

[12] G. Obara, Y. Tanaka, N. N. Nedyalkov, M. Terakawa, M. Obara, Direct observation of surface plasmon far field for regular surface ripple formation by femtosecond laser pulse irradiation of gold nanostructures on silicon substrates, Applied Physics Letters 99 (6) (2011) 061106.

[13] G. Obara, N. Maeda, T. Miyanishi, M. Terakawa, N. N. Nedyalkov, M. Obara, Plasmonic and mie scattering control of far-field interference for regular ripple formation on various material substrates, Optics Express 19 (20) (2011) 19093–19103.

[14] R. D. Murphy, B. Torralva, D. P. Adams, S. M. Yalisove, Laser-induced periodic surface structure formation resulting from single-pulse ultrafast irradiation of Au microstructures on a Si substrate, Applied Physics Letters 102 (21) (2013) 211101.

[15] T. Enami, G. Obara, M. Terakawa, M. Obara, Electron excitation effect on scattering near-field and far-field ablation material processing by femtosecond laser irradiation, Applied Physics A 114 (1) (2014) 253–259.

[16] K. Zhou, X. Jia, T. Jia, K. Cheng, K. Cao, S. Zhang, D. Feng, Z. Sun, The influences of surface plasmons and thermal effects on femtosecond laser-induced subwavelength periodic ripples on Au film by pump-probe imaging, Journal of Applied Physics 121 (10) (2017) 104301.

[17] A. Rudenko, J.-P. Colombier, S. Höhm, A. Rosenfeld, J. Krüger, J. Bonse, T. E. Itina, Spontaneous periodic ordering on the surface and in the bulk of dielectrics irradiated by ultrafast laser: a shared electromagnetic origin, Scientific Reports 7 (1) (2017) 12306.

[18] X. Sedao, A. Abou Saleh, A. Rudenko, T. Douillard, C. Esnouf, S. Reynaud, C. Maurice, F. Pigeon, F. Garrelie, J.-P. Colombier, Self-arranged periodic nanovoids by ultrafast laser-induced near-field enhancement, ACS Photonics 5 (4) (2018) 1418–1426.

[19] J. Liu, X. Jia, W. Wu, K. Cheng, D. Feng, S. Zhang, Z. Sun, T. Jia, Ultrafast imaging on the formation of periodic ripples on a Si surface with a prefabricated nanogroove induced by a single femtosecond laser pulse, Optics Express 26 (5) (2018) 6302–6315.

[20] N. Bloembergen, Role of cracks, pores, and absorbing inclusions on laser induced damage threshold at surfaces of transparent dielectrics, Applied Optics 12 (4) (1973) 661–664.

[21] J. Z. P. Skolski, G. R. B. E. Römer, J. V. Obona, V. Ocelik, A. J. Huis in 't Veld, J. T. M. De Hosson, Laser-induced periodic surface structures: Fingerprints of light localization, Phys. Rev. B 85 (2012) 075320.

[22] H. Zhang, J.-P. Colombier, C. Li, N. Faure, G. Cheng, R. Stoian, Coherence in ultrafast laser-induced periodic surface structures, Phys. Rev. B 92 (2015) 174109.

[23] G. Mie, Beiträge zur Optik trüber Medien, speziell kolloidaler Metallösungen, Annalen der Physik 330 (3) (1908) 377–445.

[24] M. Born, E. Wolf, Principles of optics: electromagnetic theory of propagation, interference and diffraction of light, Elsevier, 2013.

[25] P. A. Bobbert, J. Vlieger, Light scattering by a sphere on a substrate, Physica A: Statistical Mechanics and its Applications 137 (1-2) (1986) 209–242.

[26] G. Videen, Light scattering from a sphere on or near a surface, JOSA A 8 (3) (1991) 483–489.

[27] J. Weiner, Phase shifts and interference in surface plasmon polariton waves, Optics Express 16 (2) (2008) 950–956.

[28] H. Liu, Symmetry in the elementary scattering of surface plasmon polaritons and a generalized symmetry principle, Optics Letters 35 (17) (2010) 2876–2878.

[29] A. Klick, S. de la Cruz, C. Lemke, M. Großmann, H. Beyer, J. Fiutowski, H.-G. Rubahn, E. R. Mendez, M. Bauer, Amplitude and phase of surface plasmon polaritons excited at a step edge, Applied Physics B 122 (4) (2016) 79.

[30] P. Lalanne, J. P. Hugonin, Interaction between optical nano-objects at metallo-dielectric interfaces, Nature Physics 2 (8) (2006) 551.

[31] A. Y. Nikitin, F. J. García-Vidal, L. Martín-Moreno, Surface electromagnetic field radiated by a subwavelength hole in a metal film, Physical Review Letters 105 (7) (2010) 073902.

[32] R. E. Collin, Hertzian dipole radiating over a lossy earth or sea: some early and late 20th-century controversies, IEEE Antennas and Propagation Magazine 46 (2004) 64–79.

[33] K. S. Yee, Numerical solution of initial boundary value problems involving Maxwells equations in isotropic media, IEEE Trans. Antennas and Propagation (1966) 302–307.

[34] U. S. Inan, R. A. Marshall, Numerical electromagnetics: the FDTD method, Cambridge University Press, 2011.

[35] H. W. Kihm, J. H. Kang, J. S. Kyoung, K. G. Lee, M. A. Seo, K. J. Ahn, Separation of surface plasmon polariton from nonconfined cylindrical wave launched from single slits, Applied Physics Letters 94 (14) (2009) 141102.

[36] M. Irannejad, M. Yavuz, B. Cui, Finite difference time domain study of light transmission through multihole nanostructures in metallic film, Photonics Research 1 (4) (2013) 154–159.

[37] J. A. Roden, S. D. Gedney, et al., Convolutional PML (CPML): An efficient FDTD implementation of the CFS-PML for arbitrary media, Microwave and Optical Technology Letters 27 (5) (2000) 334–338.

[38] A. Rudenko, J.-P. Colombier, T. E. Itina, From random inhomogeneities to periodic nanostructures induced in bulk silica by ultrashort laser, Physical Review B 93 (7) (2016) 075427.

[39] A. Pors, S. I. Bozhevolnyi, Quantum emitters near layered plasmonic nanostructures: Decay rate contributions, ACS Photonics 2 (2) (2015) 228–236.

[40] J. Yang, J.-P. Hugonin, P. Lalanne, Near-to-far field transformations for radiative and guided waves, ACS

Photonics 3 (3) (2016) 395–402.
[41] P. B. Johnson, R. W. Christy, Optical constants of transition metals: Ti, V, Cr, Mn, Fe, Co, Ni, and Pd, Physical Review B 9 (12) (1974) 5056.
[42] S. E. Yalcin, Y. Wang, M. Achermann, Spectral bandwidth and phase effects of resonantly excited ultrafast surface plasmon pulses, Applied Physics Letters 93 (10) (2008) 101103.

Highlights:

1) Non-radiative patterns near surface holes and bumps are inversed
2) Far-field maxima and minima positions are inversed for holes and bumps
3) Interference maxima have opposite orientation on glass and metal surfaces
4) Interference maxima qualitatively differ for holes and voids close to surface
5) Less pronounced patterns for short pulses with finite spectral bandwidth
6) Asymmetric shape may switch the absorbed energy maxima positions
7) Multiple holes and bumps generate joint interference patterns on the surface